mathematics

MDPI

Article

Effects of LTNE on Two-Component Convective Instability in a Composite System with Thermal Gradient and Heat Source

Varalakshmi K. Balaji [1], Manjunatha Narayanappa [1,*], Ramalingam Udhayakumar [2], Ghada AlNemer [3,*], Sumithra Ramakrishna [4] and Gangadharaih Yeliyur Honnappa [5]

[1] Department of Mathematics, School of Applied Sciences, REVA University, Bengaluru 560064, India; r21pmt14@reva.edu.in
[2] Department of Mathematics, School of Advanced Sciences, Vellore Institute of Technology, Vellore 632014, India; udhayakumar.r@vit.ac.in
[3] Department of Mathematical Sciences, College of Science, Princess Nourah bint Abdulrahman University, P.O. Box 84428, Riyadh 11671, Saudi Arabia
[4] Department of Mathematics, Nrupathunga University, Bengaluru 560064, India; sumitra_diya@yahoo.com
[5] Department of Mathematics, RV Institute of Technology & Management, Bengaluru 560076, India; gangadharaiahyh.rvitm@rvei.edu.in
* Correspondence: manjunatha.n@reva.edu.in (M.N.); gnnemer@pnu.edu.sa (G.A.)

Abstract: An analytical study is conducted to examine the influence of thermal gradients and heat sources on the onset of two-component Rayleigh–Bènard (TCRB) convection using the Darcy model. The study takes into account the effects of local thermal non-equilibrium (LTNE), thermal profiles, and heat sources. The composite structure is horizontally constrained by adiabatic stiff boundaries, and the resulting solution to the problem is obtained using the perturbation approach. The various physical parameters have been thoroughly examined, revealing that the fluid layer exhibits dominance in the two-layer configuration. It has been observed that the parabolic profile demonstrates greater stability in comparison to the step function. Conversely, in the setup where the porous layer dominates, the step function plays a crucial role in maintaining stability. The porous layer, model (iv), exhibits greater stability in the predominant combined structure, while the linear configuration is characterized by higher instability.

Keywords: heat source; LTNE; two component; thermal gradients; Rayleigh–Bènard convection; corrected internal Rayleigh numbers; perturbation approach

MSC: 76R10; 76R50; 80A19

Citation: Balaji, V.K.; Narayanappa, M.; Udhayakumar, R.; AlNemer, G.; Ramakrishna, S.; Honnappa, G.Y. Effects of LTNE on Two-Component Convective Instability in a Composite System with Thermal Gradient and Heat Source. *Mathematics* **2023**, *11*, 4282. https://doi.org/10.3390/math11204282

Academic Editors: Nikolay M. Zubarev and Evgeny A. Kochurin

Received: 11 September 2023
Revised: 10 October 2023
Accepted: 10 October 2023
Published: 13 October 2023

1. Introduction

Double-component convection is very important for studying the evolution of systems with various causes of density fluctuations. Such systems occur in the sun, the oceans, and in the mantle of the Earth. Modeling of two-component convection in a composite layer can be used in many situations, including the storage of nuclear waste, thermal insulation, grain storage, chemical dispersion through water-saturated soil, and soil pollution. However, one more crucial use is for modeling the boundary conditions at interfaces. This matter has garnered significant theoretical interest due to its importance in understanding interface boundary conditions, as well as its aforementioned practical implications. The role of LTNE is significant in inflows with pronounced temperature differences between the solid phase and fluid phase. Wang et al. [1] studied solar air receiver and radiation effects using the LTNE model. Internal heat, using a local thermal non-equilibrium model, was analyzed analytically by Altawallbeh et al. [2,3] in a Maxwell fluid-porous layer with and without a magnetic field. Abidin et al. [4] conducted a study to examine the effects of viscosity in a binary fluid layer. In a two-component system, the closed form of the solution to

Marangoni convection with a magnetic field and salinity gradients was studied by Komala and Sumithra [5]. Kuznetsov and Nield [6] studied the LTNE effects for a nanofluid in the presence of a porous domain using the Darcy model. Thirupathi Thumma and Mishra [7] studied nanofluid flow over a stretching sheet in the presence of a heat source/sink using the domain decomposition method. Heat transmission in a porous medium under LTNE conditions was studied by Shashi Prabha et al. [8]. Double-component convective flow over a chemically reactive plate with a heat source/sink was investigated numerically by Kannan and Pullepu [9]. Using the LTNE model, Astanina et al. [10] studied the heat source effect for porous cavities. Hema et al. [11] used the LTNE model to investigate how heat flow affects two-component convection. Pulkit et al. [12] analyzed the phenomenon of double-diffusive convection in a rotating couple-stress ferromagnetic fluid-porous medium, taking into consideration the influence of both gravitational and magnetic fields. Shukla and Gupta [13] studied three-component convection in nanofluids using the LTNE model. Two-component convection in a combined setup with a heated and salted subsurface was investigated by Mahajan and Tripathi [14]. Meften and Ali [15] studied two-component convection with variable viscosity. Capone et al. [16,17] investigated the convection in a rotating, viscous, anisotropic porous medium in the LTNE regime. Using the Brinkmann–Forchheimer model, Meften et al. [18] examined the LTNE effects for dual-component convection with rotation. Safia et al. [19] investigated the impact of magnetic field, temperature, and concentration on convection in a nanofluid. Double diffusion of a nanofluid was investigated by Tahar et al. [20], who focused on magneto-natural convection. A stability assessment of Brinkman–Bènard convection was studied by Siddabasappa et al. [21]. Thermosolutal convection in an LTNE porous medium was examined by Noon and Haddad [22]. Corcione and Quintino [23] examined the dual-component effects for water-based nanofluids using Rayleigh–Bènard convection. Gangadharaih et al. [24] studied the gravity fluctuation and throughflow for an anisotropic porous layer. Ahmed [25] conducted a numerical study on convection in a fluid layer within a square-packed bed enclosure using the LTNE model. Atul and Anand Kumar [26] studied the effects of the solute boundary conditions and the heat source on two-component convection. Yellamma et al. [27] investigated the third-component effect for a combined system with a magnetic field, heat source, and thermal profiles. They obtained the thermal Marangoni number analytically.

Inspired by the aforementioned literature review, the current study examines the effects of LTNE in a composite layer with six thermal gradients on the onset of SCRB convection in a two-layer configuration with an incompressible horizontal fluid flow. The problem has been solved by using the perturbation technique and it is noted that the parabolic profile demonstrates greater stability in comparison to the step function. Conversely, in the setup where the porous layer dominates, the step function plays a crucial role in maintaining stability. This work undoubtedly holds tremendous potential for a multitude of applications in the fields of pure crystal growth formation, as elucidated by Rudolph et al. [28].

2. Materials and Methods

Assume a continuous horizontal layer of incompressible fluid with a thickness d_{fL} and a densely packed region-II d_{pL} of the same fluid that lies behind region-I and is heated continuously by heat sources Q_{fL} and Q_{pL} The area above region-1 is expected to be affected by surface tension effects and concentration as functions of temperature and concentration, while the area below region-II is assumed to be stable. The coordinate system used is Cartesian, with the z-axis pointing upward and the origin located at the interface between the fluid and porous layers, as shown in Figure 1. Both the solid and liquid phases are assumed to be in the LTNE, and it is thought that a solid–fluid field model can characterize the temperature differences between the solid and liquid phases separately for the porous layer.

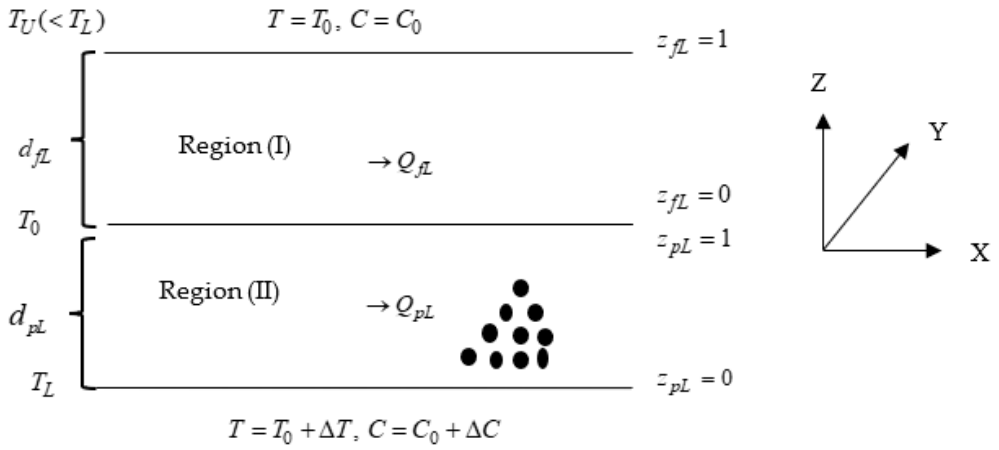

Figure 1. Model of the problem.

For the composite system Darcy model, the basic equations assume the Boussinesq hypothesis (see Sumithra and Shyamala [29]).

Fluid layer (region-I):

$$\nabla_{fL}\cdot\vec{q}_{fL}=0 \tag{1}$$

$$\begin{aligned}\frac{\partial\vec{q}_{fL}}{\partial t_{fL}}+\left(\vec{q}_{fL}\cdot\nabla_{fL}\right)\vec{q}_{fL}=&-\frac{\nabla_{fL}P_{fL}}{\rho_0}+\frac{\mu_{fL}}{\rho_0}\nabla_{fL}^2\vec{q}_{fL}\\&-\left[1-\alpha_{fL}(T_{fL}-T_{fL0})+\alpha_{fLs}(C_{fL}-C_{fL0})\right]g\,\hat{k}\end{aligned} \tag{2}$$

$$\frac{\partial T_{fL}}{\partial t}+\left(\vec{q}_{fL}\cdot\nabla_{fL}\right)T_{fL}=\kappa_{fL}\nabla_{fL}^2T_{fL}+Q_{fL} \tag{3}$$

$$\frac{\partial C_{fL}}{\partial t}+\left(\vec{q}_{fL}\cdot\nabla_{fL}\right)C_{fL}=\kappa_{fLs}\nabla_{fL}^2C_{fL} \tag{4}$$

The porous layer (region-II) (see Nield and Bejan [30]):

$$\nabla_{pL}\cdot\vec{q}_{pL}=0 \tag{5}$$

$$\begin{aligned}\phi^{-1}\frac{\partial\vec{q}_{pL}}{\partial t_{pL}}+\phi^{-2}\left(\vec{q}_{pL}\cdot\nabla_{pL}\right)\vec{q}_{pL}=&-\frac{\nabla_{pL}P_{pL}}{\rho_0}+\frac{\mu_{pL}}{K\rho_0}\vec{q}_{pL}\\-\left[1-\alpha_{fpL}(T_{fpL}-T_{pL0})-\alpha_{spL}(T_{spL}-T_{pL0})+\alpha_{pL}(C_{pL}-C_{pL0})\right]&g\,\hat{k}\end{aligned} \tag{6}$$

$$(\rho c_p)_{fpL}\left[\phi\frac{\partial T_{fpL}}{\partial t_{pL}}+\left(\vec{q}_{pL}\cdot\nabla_{pL}\right)T_{fpL}\right]=\phi\kappa_{fpL}\nabla_{pL}^2T_{fpL}+h(T_{spL}-T_{fpL})+Q_{pL} \tag{7}$$

$$(1-\phi)(\rho c_p)_{spL}\frac{\partial T_{spL}}{\partial t_{pL}}=(1-\phi)\kappa_{spL}\nabla_{pL}^2T_{spL}-h\left(T_{spL}-T_{fpL}\right) \tag{8}$$

$$\phi\frac{\partial C_{pL}}{\partial t_{pL}}+\left(\vec{q}_{pL}\cdot\nabla_{pL}\right)C_{pL}=\kappa_{pLs}\nabla_{pL}^2C_{pL} \tag{9}$$

For the two regions, the basic state is expressed as follows:

$$\begin{aligned}&\left[\vec{q}_{fL},P_{fL},T_{fL},T_{sfL},C_{fL}\right]\\&=\left[0,P_{fLb}(z_{fL}),T_{fLb}(z_{fL}),T_{sfLb}(z_{fL}),C_{fLb}(z_{fL})\right],\frac{-d_{fL}}{\Delta T}\frac{dT_{fLb}}{dz_{fL}}=F_{fL}(z_{fL})\end{aligned} \tag{10}$$

$$\begin{aligned}&\left[\vec{q}_{pL}, P_{pL}, T_{fpL}, T_{spL}, C_{pL}\right]\\&= \left[0, P_{pLb}(z_{pL}), T_{fpLb}(z_{pL}), T_{spLb}(z_{pL}), C_{pLb}(z_{pL})\right], \frac{-d_{pL}}{\Delta T}\frac{dT_{pLb}}{dz_{pL}} = F_{pL}(z_{pL})\end{aligned} \tag{11}$$

The basic state salinity and temperature distributions are, respectively, found to be:

$$T_{fLb}(z_{fL}) = \frac{Q_{fL}z_{fL}(z_{fL}-d_{fL})}{2\kappa_{fL}} + \left(\frac{T_U - T_0}{d_{fL}}\right)F_{fL}(z_{fL}) + T_0 \quad 0 \le z_{fL} \le d_{fL}$$

$$T_{fpLb}(z_{pL}) = T_{spLb}(z_{pL}) = \frac{Q_{pL}z_{pL}(z_{pL}+d_{pL})}{2\phi\kappa_{pL}} + \left(\frac{T_L - T_0}{d_{pL}}\right)F_{pL}(z_{pL}) + T_0 \quad 0 \le z_{pL} \le d_{pL}$$

$$C_{fLb}(z_{fL}) = \left(\frac{C_U - C_0}{d_{fL}}\right)z_{fL} + C_0 \quad 0 \le z_{fL} \le d_{fL}$$

$$C_{pLb}(z_{pL}) = \left(\frac{C_L - C_0}{d_{pL}}\right)z_{pL} + C_0 \quad 0 \le z_{pL} \le d_{pL}$$

$$\text{Here, } T_0 = \frac{\kappa_{fL}d_{pL}T_u + \kappa_{pL}d_{fL}T_L}{\kappa_{fL}d_{pL} + \kappa_{pL}d_{fL}} + \frac{d_{fL}d_{pL}\left(Q_{fL}d_{fL} + Q_{pL}d_{pL}\right)}{2\left(\kappa_{fL}d_{pL} + \kappa_{pL}d_{fL}\right)}$$

$$C_0 = \frac{\kappa_{fLs}C_U d_{pL} + \kappa_{pLs}C_L d_{fL}}{\kappa_{pLs}d_{fL} + \kappa_{fLs}d_{pL}}.$$

where the 'b' symbolizes the basic state, and $F_{fL}(z_{fL})$ and $F_{pL}(z_{pL})$ are the non-dimensionalized thermal gradient that fulfils the situation $\int_0^1 F_{fL}(z_{fL})\ dz_{fL} = \int_0^1 F_{pL}(z_{pL})\ dz_{pL} = 1$.

To study the basic solution's stability, the following mild disturbances are introduced.

$$\left[\vec{q}_{fL}, P_{fL}, T_{fL}, C_{fL}\right] = \left[0, P_{fLb}(z_{fL}), T_{fLb}(z_{fL}), C_{fLb}(z_{fL})\right] + \left[\vec{q}'_{fL}, \vec{P}'_{fL}, \theta, S\right] \tag{12}$$

$$\begin{aligned}\left[\vec{q}_{pL}, P_{pL}, T_{fpL}, T_{spL}, C_{pL}\right] = &\left[0, P_{pLb}(z_{pL}), T_{pLb}(z_{pL}), T_{spLb}(z_{pL}), C_{pLsb}(z_{pL})\right]\\&+\left[\vec{q}'_{pL}, \vec{P}'_{pL}, \theta_{pL}, \theta_{spL}, S_{pL}\right]\end{aligned} \tag{13}$$

The prime symbol represents a perturbation from the corresponding values at equilibrium. The physical values in Equations (1)–(9) are now augmented with the introduction of (12) and (13), and subsequently linearized based on convection. The pressure term is subsequently eliminated from Equations (2) and (6) through the application of the curl operation twice, while retaining only the upright factor.

The variables are non-dimensionalized and normal mode study is applied (see Yellamma et al. [31]); the corresponding distinctive quantities are found to be:

In $0 \le z_{fL} \le 1$,

$$\left(D_{fL}^2 - a_{fL}^2\right)^2 W_{fL} = R_{fL}a_{fL}^2\theta_{fL} - R_{fLs}a_{fL}^2 S_{fL} \tag{14}$$

$$\left(D_{fL}^2 - a_{fL}^2\right)^2 \theta_{fL} + \left[F_{fL}(z_{fL}) + R_I^*\left(2z_{fL} - 1\right)\right]W_{fL} = 0 \tag{15}$$

$$\tau_{fLs}\left(D_{fL}^2 - a_{fL}^2\right)^2 S_{fL} + W_{fL} = 0 \tag{16}$$

In $0 \le z_{pL} \le 1$,

$$\left(D_{pL}^2 - a_{pL}^2\right)^2 W_{pL} = -R_{fpL}\beta^2 a_{pL}^2 \theta_{fpL} - \tau_{spL} R_{spL}\beta^2 a_{pL}^2 \theta_{spL} + \tau_{pLs} R_{pLs}\beta^2 a_{pL}^2 S_{pL} \quad (17)$$

$$\phi\left(D_{pL}^2 - a_{pL}^2\right)\theta_{fpL} + \left[F_{pL}(z_{pL}) + R_{IM}^*(2z_{pL}+1)\right] w_{pL} = -H\left(\theta_{spL} - \theta_{fpL}\right) \quad (18)$$

$$(1-\phi)\left(D_{pL}^2 - a_{pL}^2\right)\theta_{spL} = H\left(\theta_{spL} - \theta_{fpL}\right) \quad (19)$$

$$\tau_{pLs}\left(D_{pL}^2 - a_{pL}^2\right)^2 S_{pL} + W_{pL} = 0 \quad (20)$$

where $R_{fL} = \frac{g\alpha_{fL}(T_0 - T_U)d_{fL}^3}{\nu_{fL}\kappa_{fL}}$, $R_{pL} = \frac{g\alpha_{pL}(T_L - T_0)d_{pL}^3}{\nu_{pL}\kappa_{pL}}$, $R_{fLs} = \frac{g\alpha_{fLs}(C_0 - C_U)d_{fL}^3}{\nu_{fL}\kappa_{fLs}}$, $R_{pLs} = \frac{g\alpha_{pLs}(C_L - C_0)d_{pL}^3}{\nu_{pL}\kappa_{pLs}}$, $R_{spL} = \frac{g\alpha_{spL}(T_L - T_0)d_{pL}^3}{\nu_{pL}\kappa_{spL}}$ are, respectively, the thermal, solute, and solid phase Rayleigh numbers, $R_I = \frac{Q_{fL}d_{fL}^2}{\kappa_{fL}}$, $R_{IM} = \frac{Q_{pL}d_{pL}^2}{\kappa_{fpL}}$, $R_I^* = \frac{R_I}{2(T_0 - T_U)}$, $R_{IM}^* = \frac{R_{IM}}{2(T_L - T_0)}$, $\beta^2 = \frac{K}{d_{pL}^2} = Da$, $H = \frac{hd_{pL}^3}{\kappa_{fpL}}$ are the internal and corrected Rayleigh numbers, the Darcy number, and the inter-phase heat transfer coefficient, respectively; α_{fpL}, α_{spL} are the fluid and solid phase thermal expansion coefficients; κ_{fpL}, κ_{spL} are the fluid phase and solid phase thermal diffusivities; and κ_{fLs}, κ_{pLs} are the fluid and porous layer solute diffusivities (see nomenclature).

After non-dimensionalization, normal mode expansion is carried out on the proper boundary conditions.

At $z_{fL} = d_{fL}$, the situations are

$$W_{fL}(1) = 0, D_{fL}W_{fL}(1) = 0, D_{fL}\theta_{fL}(1) = 0, D_{fL}S_{fL}(1) = 0$$

At $z_{pL} = d_{pL}$, the situations are

$$W_{pL}(0) = 0,\ D_{pL}W_{pL}(0) = 0,\ D_{pL}\theta_{fpL}(0) = 0,\ D_{pL}\theta_{spL}(0) = 0,\ D_{pL}S_{pL}(0) = 0$$

At $z_{fL} = 0$, $z_{pL} = 1$, the situations are

$$\hat{T}W_{fL}(0) = \hat{d}^2 W_{pL}(1),\ \hat{T}D_{fL}W_{fL}(0) = \hat{d}\hat{\mu}D_{pL}W_{pL}(1),$$

$$\theta_{fL}(0) = \hat{T}\hat{d}^2\theta_{fpL}(1),\ \theta_{fL}(0) = \hat{T}\hat{d}^2\theta_{spL}(1),$$

$$D_{fL}\theta_{fL}(0) = \hat{d}^2 D_{pL}\,\theta_{fpL}(1),\ D_{fL}\theta_{fL}(0) = \hat{d}^2 D_{pL}\theta_{spL}(1),$$

$$S_{fL}(0) = \hat{S}\,S_{pL}(1),\ D_{fL}S_{fL}(0) = D_{pL}S_{pL}(1),$$

$$\hat{T}\hat{d}\beta^2 D_{fL}^3 W_{fL}(0) = -D_{pL}W_{pL}(1) + \hat{\mu}\,\beta^2 D_{pL}^3 W_{pL}(1),$$

$$\hat{T}D_{fL}^2 W_{fL}(0) = \hat{\mu}D_{pL}^2 W_{pL}(1).$$

where $\hat{T} = \frac{(T_L - T_0)}{(T_0 - T_U)}$, $\hat{S} = \frac{C_L - C_0}{C_0 - C_U}$, $\hat{d} = \frac{d_{pL}}{d_{fL}}$, and $\hat{\mu} = \frac{\mu_{pL}}{\mu_{fL}}$ are the thermal, salinity, depth, and viscosity ratio, respectively.

3. Method of Solution

The task at hand involves addressing the eigenvalue problem within the context of arbitrary boundary conditions related to temperature and concentration. This will be accomplished by employing the standard perturbation method, with the wave number a_{fL}^2, a_{pL}^2 serving as the perturbation parameter. The results of such a study can be used to assess the reliability of the method, and they can also be used to justify the method's application to the solution of problems involving convective instability in which the critical stability parameter must be determined analytically.

The powers a_{fL}^2, a_{pL}^2 have been added to the dependent variables in both levels, as seen below:

$$\begin{bmatrix} W_{fL} \\ \theta_{fL} \\ S_{fL} \end{bmatrix} = \sum_{j=0}^{\infty} a_{fL}^{2j} \begin{bmatrix} W_{fLj} \\ \theta_{fLj} \\ S_{fLj} \end{bmatrix} \text{ and } \begin{bmatrix} W_{pL} \\ \theta_{fpL} \\ \theta_{spL} \\ S_{pL} \end{bmatrix} = \sum_{j=0}^{\infty} a_{pL}^{2j} \begin{bmatrix} W_{pLj} \\ \theta_{fpLj} \\ \theta_{spLj} \\ S_{pLj} \end{bmatrix} \tag{21}$$

When solving a_{fL}^2, a_{pL}^2 using the preceding equation in (14)–(20), we obtain zero-order expressions (see Appendix A).

The first-order equations for a_{fL}^2, a_{pL}^2 are as follows:

For region-I,

$$D_{fL}^4 W_{fL1} - R_{fL}\hat{T} + R_{fLs}\hat{S} = 0 \tag{22}$$

$$D_{fL}^2 \theta_{fL1} - \hat{T} + \left[F_{fL}\left(z_{fL}\right) + R_I^*\left(2z_{fL} - 1\right)\right] W_{fL1} = 0 \tag{23}$$

$$\tau_{fLs} D_{fL}^2 S_{fL1} - \tau_{fLs}\hat{S} + W_{fL1} = 0 \tag{24}$$

For region-II,

$$D_{pL}^2 W_{pL1} + R_{fpL}\beta^2 + \tau_{spL} R_{spL}\beta^2 - \tau_{pLs} R_{pLs}\beta^2 = 0 \tag{25}$$

$$\left(\phi D_{pL}^2 - H\right)\theta_{fpL1} + H\theta_{spL1} + \left[F_{pL}(z_{pL}) + R_{IM}^*(2z_{pL} + 1)\right] W_{pL1} - \phi = 0 \tag{26}$$

$$\left[(1-\phi) D_{pL}^2 - H\right]\theta_{spL1} + H\theta_{pL1} - (1-\phi) = 0 \tag{27}$$

$$\tau_{pLs} D_{pL}^2 S_{pL} - \tau_{pLs} + W_{pL} = 0 \tag{28}$$

The related boundary conditions are as follows:

$$W_{fL1}(1) = 0, D_{fL1} W_{fL1}(1) = 0, D_{fL1}\theta_{fL1}(1) = 0, D_{fL1} S_{fL1}(1) = 0,$$

$$\hat{T} W_{fL1}(0) = \hat{d}^2 W_{pL1}(1),\ \hat{T} D_{fL} W_{fL1}(0) = \hat{d}\hat{\mu} D_{pL} W_{pL1}(1),$$

$$\theta_{fL1}(0) = \hat{T}\hat{d}^2\theta_{pL1}(1),\ \theta_{fL1}(0) = \hat{T}\hat{d}^2\theta_{spL1}(1), S_{fL1}(0) = \hat{S}\hat{d}^2 S_{pL1}(1),$$

$$D_{fL}\theta_{fL1}(0) = \hat{d}^2 D_{pL}\theta_{fpL1}(1), D_{fL}\theta_{fL1}(0) = \hat{d}^2 D_{pL}\theta_{spL1}(1), D_{fL} S_{fL1}(0) = \hat{d}^2 D_{pL} S_{pL1}(1),$$

$$\hat{T}\hat{d}\beta^2 D_{fL}^3 W_{fL1}(0) = -D_{pL} W_{pL1}(1) + \hat{\mu}\beta^2 D_{pL}^3 W_{pL1}(1),\ \hat{T} D_{fL}^2 W_{fL1}(0) = \hat{\mu} D_{pL}^2 W_{pL1}(1),$$

$$W_{pL1}(0) = 0,\ D_{pL}W_{pL1}(0) = 0,\ D_{pL}\theta_{fpL1}(0) = 0,\ D_{pL}\theta_{spL1}(0) = 0, D_{pL}S_{pL1}(0) = 0.$$

The solutions of W_{fL1} and W_{pL1} are as follows:

$$W_{fL1}\,(z_{fL}) = \delta_{fL1} + \delta_{fL2}\,z_{fL} + \delta_{fL3}\,z_{fL}^2 + \delta_{fL4}\ \ z_{fL}^3 + \frac{(R_{fL}\hat{T} - R_{fLs}\hat{S})}{24} z_{fL}^4 \tag{29}$$

$$W_{pL1}(z_{pL}) = \delta_{pL5} + \delta_{pL6}\,z_{pL} - \frac{\beta^2\left(R_{fpL} + R_{spL}\,\tau_{spL} - R_{pLs}\,\tau_{pLs}\right)}{2} z_{pL}^2 \tag{30}$$

where $\delta_{fL1}, \delta_{fL2}, \delta_{fL3}, \delta_{fL4}, \delta_{fL5}, \delta_{fL6}$ are the constants obtained utilizing velocity boundary conditions; for the form they are in, see Appendix A.

4. Condition of Solvability

The solvability condition is derived by solving the differential equation with the necessary boundary conditions concerning heat.

$$\begin{aligned} \hat{d}^2\left(1 + R_{IM}^* + \tau_{fLs}\right)\int_0^1 W_{pL1}(z_{pL})\cdot F_{pL}(z_{pL})\,dz_{pL} + 2\hat{d}^2 R_{IM}^*\int_0^1 W_{pL1}(z_{pL})\cdot F_{pL}(z_{pL})\,dz_{pL} \\ +\left(1 - R_I^* + \tau_{pLs}\right)\int_0^1 W_{fL1}(z_{fL})\cdot F_{fL}(z_{fL})\,dz_{fL} + 2R_I^*\int_0^1 W_{fL1}(z_{fL})\cdot F_{fL}(z_{fL})\,dz_{fL} \\ = \left(\hat{d}^2 + \hat{T}\right) + \left(\hat{d}^2 + \hat{S}\right)\tau_{fLs}\tau_{pLs} \end{aligned} \tag{31}$$

Computing R_C for different profiles can be achieved by substituting expressions $W_{fL1}(z_{fL})$ and $W_{pL1}(z_{pL})$ from Equations (29) and (30) into Equation (31).

5. Thermal Gradients

The following thermal gradients are considered for the present study (refer to Table 1; see Rudraiah et al. [32], Vasseur and Robillard [33], and Shivakumara [34]).

Table 1. Thermal gradients for fluid and porous layer.

Model	Thermal Gradients	Fluid Layer (Region-I)	Porous Layer (Region-II)
Model (i)	Linear	$F_{fL}(z_{fL}) = 1$	$F_{pL}(z_{pL}) = 1$
Model (ii)	Parabolic	$F_{fL}(z_{fL}) = 2z_{fL}$	$F_{pL}(z_{pL}) = 2z_{pL}$
Model (iii)	Inverted parabolic	$F_{fL}(z_{fL}) = 2(1 - z_{fL})$	$F_{pL}(z_{pL}) = 2(1 - z_{pL})$
Model (iv)	Piecewise linear gradient heated from below (PLHB)	$F_{fL}(z_{fL}) = \begin{cases} \varepsilon_{fL}^{-1}, & 0 \le z_{fL} \le \varepsilon_{fL} \\ 0, & \varepsilon_{fL} \le z_{fL} \le 1 \end{cases}$	$F_{pL}(z_{pL}) = \begin{cases} \varepsilon_{pL}^{-1}, & 0 \le z_{pL} \le \varepsilon_{pL} \\ 0, & \varepsilon_{pL} \le z_{pL} \le 1 \end{cases}$
Model (v)	Piecewise linear gradient cooled from above (PLCA)	$F_{fL}(z_{fL}) = \begin{cases} 0, & 0 \le z_{fL} \le (1 - \varepsilon_{fL}) \\ \varepsilon_{fL}^{-1}, & (1 - \varepsilon_{fL}) \le z_{fL} \le 1 \end{cases}$	$F_{pL}(z_{pL}) = \begin{cases} 0, & 0 \le z_{pL} \le (1 - \varepsilon_{pL}) \\ \varepsilon_{pL}^{-1}, & (1 - \varepsilon_{pL}) \le z_{pL} \le 1 \end{cases}$
Model (vi)	Step function (SF)	$F_{fL}(z_{fL}) = \delta\left(z_{fL} - \varepsilon_{fL}\right)$	$F_{pL}(z_{pL}) = \delta(z_{pL} - \varepsilon_{pL})$

5.1. Model (i): Linear Thermal Gradient

The R_C is attained for the linear model $F_{fL}(z_{fL}) = 1$ and $F_{pL}(z_{pL}) = 1$ by utilizing (31):

$$R_C = \frac{\left(\hat{d}^2 + \hat{T}\right) + \left(\hat{d}^2 + \hat{S}\right)\tau_{fLs}\tau_{pLs} - \hat{d}^4\kappa_{pLs}^2\tau_{pLs}\Psi_1 - R_{pLs}\{\Phi_{11} + \Phi_{12}\}}{\hat{T}\{\Phi_{13} + \Phi_{14}\} + \left[\alpha_{fpL}\,\kappa_{fpL}^2 + \alpha_{spL}\kappa_{spL}^2\tau_{spL}\right]\hat{d}^4\,\Psi_1} \tag{32}$$

where $\Psi_1 = \Phi_1 + \Phi_2 + \Phi_3 + \Phi_4 + \Phi_5 + \Phi_6 + \Phi_7 + \Phi_8 + \Phi_9 + \Phi_{10}$, $\Phi_1 = \frac{\hat{d}^2\beta^2\left(1+R_{IM}^*+\tau_{fLs}\right)}{6}$, $\Phi_2 = \frac{\hat{d}^2\beta^2 R_{IM}^*}{4}$, $\Phi_3 = \frac{\hat{d}^2\beta^2\left(1-R_I^*+\tau_{pLs}\right)}{2}$, $\Phi_4 = \frac{\hat{d}\beta^2\hat{\mu}\left(1-R_I^*+\tau_{pLs}\right)}{2\hat{T}}$, $\Phi_5 = \frac{\beta^2\hat{\mu}\left(1-R_I^*+\tau_{pLs}\right)}{6\hat{T}}$, $\Phi_6 = \frac{\left(1-R_I^*+\tau_{pLs}\right)}{24\hat{d}\hat{T}}$, $\Phi_7 = \frac{\hat{d}^2\beta^2 R_I^*}{2\hat{T}}$, $\Phi_8 = \frac{2\hat{d}\beta^2\hat{\mu}R_I^*}{3\hat{T}}$, $\Phi_9 = \frac{\beta^2\hat{\mu}R_I^*}{4\hat{T}}$, $\Phi_{10} = \frac{R_I^*}{15\hat{d}\hat{T}}$, $\Phi_{11} = \frac{\hat{S}\left(1-R_I^*+\tau_{pLs}\right)}{120}$, $\Phi_{12} = \frac{2\hat{S}R_I^*}{144}$, $\Phi_{13} = \frac{\left(1-R_I^*+\tau_{pLs}\right)}{120}$, $\Phi_{14} = \frac{2R_I^*}{144}$.

5.2. Model (ii): Parabolic Thermal Gradient

The R_C is attained for the parabolic model $F_{fL}(z_{fL}) = 2z_{fL}$, $F_{pL}(z_{pL}) = 2z_{pL}$ by utilizing (31):

$$R_C = \frac{\left(\hat{d}^2 + \hat{T}\right) + \left(\hat{d}^2 + \hat{S}\right)\tau_{fLs}\tau_{pLs} - \hat{d}^4\kappa_{pLs}^2\tau_{pLs}\Psi_2 - R_{pLs}\{\mathrm{N}_{11} + \mathrm{N}_{12}\}}{\hat{T}\{\mathrm{N}_{13} + \mathrm{N}_{14}\} + \left[\alpha_{fpL}\,\kappa_{fpL}^2 + \alpha_{spL}\kappa_{spL}^2\tau_{spL}\right]\hat{d}^4\,\Psi_2} \tag{33}$$

where $\Psi_2 = \mathrm{N}_1 + \mathrm{N}_2 + \mathrm{N}_3 + \mathrm{N}_4 + \mathrm{N}_5 + \mathrm{N}_6 + \mathrm{N}_7 + \mathrm{N}_8 + \mathrm{N}_9 + \mathrm{N}_{10}$, $\mathrm{N}_1 = \frac{\hat{d}^2\beta^2\left(1+R_{IM}^*+\tau_{fLs}\right)}{4}$, $\mathrm{N}_2 = \frac{2\hat{d}^2\beta^2 R_{IM}^*}{5}$, $\mathrm{N}_3 = \frac{\hat{d}^2\beta^2\left(1-R_I^*+\tau_{pLs}\right)}{2\hat{T}}$, $\mathrm{N}_4 = \frac{2\hat{d}\hat{\mu}\beta^2\left(1-R_I^*+\tau_{pLs}\right)}{3\hat{T}}$, $\mathrm{N}_5 = \frac{\beta^2\hat{\mu}\left(1-R_I^*+\tau_{pLs}\right)}{4\hat{T}}$, $\mathrm{N}_6 = \frac{\left(1-R_I^*+\tau_{pLs}\right)}{15\hat{d}\hat{T}}$, $\mathrm{N}_7 = \frac{3\hat{d}^2\beta^2 R_I^*}{3\hat{T}}$, $\mathrm{N}_8 = \frac{\hat{d}\beta^2\hat{\mu}R_I^*}{\hat{T}}$, $\mathrm{N}_9 = \frac{2\beta^2\hat{\mu}R_I^*}{5\hat{T}}$, $\mathrm{N}_{10} = \frac{R_I^*}{9\hat{d}\hat{T}}$, $\mathrm{N}_{11} = \frac{\hat{S}\left(1-R_I^*+\tau_{pLs}\right)}{72}$, $\mathrm{N}_{12} = \frac{\hat{S}R_I^*}{42}$, $\mathrm{N}_{13} = \frac{\left(1-R_I^*+\tau_{pLs}\right)}{72}$, $\mathrm{N}_{14} = \frac{R_I^*}{42}$.

5.3. Model (iii): Inverted Parabolic Thermal Gradient

The R_C is attained for this model $F_{fL}(z_{fL}) = 2(1 - z_{fL})$ and $F_{pL}(z_{pL}) = 2(1 - z_{pL})$ by utilizing (31):

$$R_C = \frac{\left(\hat{d}^2 + \hat{T}\right) + \left(\hat{d}^2 + \hat{S}\right)\tau_{fLs}\tau_{pLs} - \hat{d}^4\kappa_{pLs}^2\tau_{pLs}\Psi_3 - R_{pLs}\{\mathrm{A}_{11} + \mathrm{A}_{12}\}}{\hat{T}\{\mathrm{A}_{13} + \mathrm{A}_{14}\} + \left[\alpha_{fpL}\,\kappa_{fpL}^2 + \alpha_{spL}\kappa_{spL}^2\tau_{spL}\right]\hat{d}^4\;\Psi_3} \tag{34}$$

where $\Psi_3 = \mathrm{A}_1 + \mathrm{A}_2 + \mathrm{A}_3 + \mathrm{A}_4 + \mathrm{A}_5 + \mathrm{A}_6 + \mathrm{A}_7 + \mathrm{A}_8 + \mathrm{A}_9 + \mathrm{A}_{10}$, $\mathrm{A}_1 = \frac{\hat{d}^2\beta^2\left(1+R_{IM}^*+\tau_{fLs}\right)}{12}$, $\mathrm{A}_2 = \frac{\hat{d}^2\beta^2 R_{IM}^*}{10}$, $\mathrm{A}_3 = \frac{\hat{d}^2\beta^2\left(1-R_I^*+\tau_{pLs}\right)}{2\hat{T}}$, $\mathrm{A}_4 = \frac{\hat{d}\beta^2\hat{\mu}\left(1-R_I^*+\tau_{pLs}\right)}{3\hat{T}}$ $\mathrm{A}_5 = \frac{\beta^2\hat{\mu}\left(1-R_I^*+\tau_{pLs}\right)}{12\hat{T}}$, $\mathrm{A}_6 = \frac{\left(1-R_I^*+\tau_{pLs}\right)}{60\hat{d}\hat{T}}$, $\mathrm{A}_7 = \frac{\hat{d}^2\beta^2 R_I^*}{3\hat{T}}$, $\mathrm{A}_8 = \frac{\hat{d}\beta^2\hat{\mu}R_I^*}{3\hat{T}}$, $\mathrm{A}_9 = \frac{\beta^2\hat{\mu}R_I^*}{10\hat{T}}$, $\mathrm{A}_{10} = \frac{R_I^*}{45\hat{d}\hat{T}}$, $\mathrm{A}_{11} = \frac{\hat{S}\left(1-R_I^*+\tau_{pLs}\right)}{360}$, $\mathrm{A}_{12} = \frac{\hat{S}R_I^*}{252}$, $\mathrm{A}_{13} = \frac{\left(1-R_I^*+\tau_{pLs}\right)}{360}$, $\mathrm{A}_{14} = \frac{R_I^*}{252}$.

5.4. Model (iv): Piecewise Linear Gradient Heated from Below

$$F_{fL}(z_{fL}) = \begin{cases} \varepsilon_{fL}^{-1}, & 0 \le z_{fL} \le \varepsilon_{fL} \\ 0, & \varepsilon_{fL} \le z_{fL} \le 1 \end{cases} \text{ and } F_{pL}(z_{pL}) = \begin{cases} \varepsilon_{pL}^{-1}, & 0 \le z_{pL} \le \varepsilon_{pL} \\ 0, & \varepsilon_{pL} \le z_{pL} \le 1 \end{cases} \tag{35}$$

The R_c is attained for this model by utilizing (35) in (31) and is calculated as follows:

$$R_C = \frac{\left(\hat{d}^2 + \hat{T}\right) + \left(\hat{d}^2 + \hat{S}\right)\tau_{fLs}\tau_{pLs} - \hat{d}^4\kappa_{pLs}^2\tau_{pLs}\Psi_4 - R_{pLs}\{\mathrm{B}_{11} + \mathrm{B}_{12}\}}{\hat{T}\{\mathrm{B}_{13} + \mathrm{B}_{14}\} + \left[\alpha_{fpL}\,\kappa_{fpL}^2 + \alpha_{spL}\kappa_{spL}^2\tau_{spL}\right]\hat{d}^4\;\Psi_4} \tag{36}$$

where $\Psi_4 = \mathrm{B}_1 + \mathrm{B}_2 + \mathrm{B}_3 + \mathrm{B}_4 + \mathrm{B}_5 + \mathrm{B}_6 + \mathrm{B}_7 + \mathrm{B}_8 + \mathrm{B}_9 + \mathrm{B}_{10}$, $\mathrm{B}_1 = \frac{\hat{d}^2\beta^2\left(1+R_{IM}^*+\tau_{fLs}\right)\varepsilon_{pL}^2}{6}$, $\mathrm{B}_2 = \frac{\hat{d}^2\beta^2 R_{IM}^*\varepsilon_{pL}^3}{4}$, $\mathrm{B}_3 = \frac{\hat{d}^2\beta^2\left(1-R_I^*+\tau_{pLs}\right)}{2\hat{T}}$, $\mathrm{B}_4 = \frac{\hat{d}\beta^2\mu_{fL}\left(1+R_I^*+\tau_{pLs}\right)\varepsilon_{fL}}{2\hat{T}}$ $\mathrm{B}_5 = \frac{\beta^2\hat{\mu}\left(1-R_I^*+\tau_{pLs}\right)\varepsilon_{fL}^2}{6\hat{T}}$,

$$B_6 = \frac{\left(1-R_I^*+\tau_{pLs}\right)\varepsilon_{fL}^3}{24\hat{d}\hat{T}}, B_7 = \frac{\hat{d}^2\beta^2 R_I^*\varepsilon_{fL}}{2\hat{T}}, B_8 = \frac{2\hat{d}\beta^2\hat{\mu}R_I^*\varepsilon_{fL}^2}{3\hat{T}}, B_9 = \frac{\beta^2\hat{\mu}R_I^*\varepsilon_{fL}^3}{4\hat{T}}, B_{10} = \frac{R_I^*\varepsilon_{fL}^4}{15\hat{d}\hat{T}},$$
$$B_{11} = \frac{\hat{S}\left(1-R_I^*+\tau_{pLs}\right)\varepsilon_{fL}^4}{120}, B_{12} = \frac{\hat{S}R_I^*\varepsilon_{fL}^5}{72}, B_{13} = \frac{\left(1-R_I^*+\tau_{pLs}\right)\varepsilon_{fL}^4}{120}, B_{14} = \frac{R_I^*\varepsilon_{fL}^5}{72}.$$

5.5. Model (v): Piecewise Linear Gradient Cooled from Above

$$F_{fL}(z_{fL}) = \begin{cases} 0, & 0 \le z_{fL} \le \left(1-\varepsilon_{fL}\right) \\ \varepsilon_{fL}^{-1}, & \left(1-\varepsilon_{fL}\right) \le z_{fL} \le 1 \end{cases} \text{ and } F_{pL}(z_{pL}) = \begin{cases} 0, & 0 \le z_{pL} \le (1-\varepsilon_{pL}) \\ \varepsilon_{pL}^{-1}, & (1-\varepsilon_{pL}) \le z_{pL} \le 1 \end{cases} \tag{37}$$

The R_c is attained for this model by utilizing (37) in (31) and is calculated as follows:

$$R_C = \frac{\left(\hat{d}^2+\hat{T}\right)+\left(\hat{d}^2+\hat{S}\right)\tau_{fLs}\tau_{pLs}-\hat{d}^4\kappa_{pLs}^2\tau_{pLs}\Psi_5-R_{pLs}\{\mathbb{R}_{11}+\mathbb{R}_{12}\}}{\hat{T}\{\mathbb{R}_{13}+\mathbb{R}_{14}\}+\left[\alpha_{fpL}\,\kappa_{fpL}^2+\alpha_{spL}\kappa_{spL}^2\tau_{spL}\right]\hat{d}^4\;\Psi_5} \tag{38}$$

where $\Psi_5 = \mathbb{R}_1+\mathbb{R}_2+\mathbb{R}_3+\mathbb{R}_4+\mathbb{R}_5+\mathbb{R}_6+\mathbb{R}_7+\mathbb{R}_8+\mathbb{R}_9+\mathbb{R}_{10}$, $\mathbb{R}_1 = \frac{\hat{d}^2\beta^2\left(1+R_{IM}^*+\tau_{fLs}\right)}{2\varepsilon_{pL}}$ $\frac{\left(1-(1-\varepsilon_{fL})^3\right)}{3}$, $\mathbb{R}_2 = \frac{\hat{d}^2\beta^2 R_{IM}^*}{\varepsilon_{pL}}\frac{\left(1-(1-\varepsilon_{pL})^4\right)}{4}$, $\mathbb{R}_3 = \frac{\hat{d}^2\beta^2\left(1-R_I^*+\tau_{pLs}\right)}{2}$, $\mathbb{R}_4 = \frac{\hat{d}\beta^2\hat{\mu}\left(1+R_I^*+\tau_{pLs}\right)}{2\hat{T}\varepsilon_{fL}}$, $\mathbb{R}_5 = \frac{\beta^2\hat{\mu}\left(1-R_I^*+\tau_{pLs}\right)\left(1-\left(1-\varepsilon_{fL}\right)^3\right)}{6\hat{T}\varepsilon_{fL}}$, $\mathbb{R}_6 = \frac{\left(1-R_I^*+\tau_{pLs}\right)\left(1-\left(1-\varepsilon_{fL}\right)^4\right)}{24\hat{d}\hat{T}\varepsilon_{fL}}$, $\mathbb{R}_7 = \frac{\hat{d}^2\beta^2 R_I^*\left(1-\left(1-\varepsilon_{fL}\right)^2\right)}{2\varepsilon_{fL}\hat{T}}$, $\mathbb{R}_8 = \frac{2\hat{d}\beta^2\hat{\mu}R_I^*\left(1-\left(1-\varepsilon_{fL}\right)^3\right)}{3\hat{T}_{\varepsilon fL}}$, $\mathbb{R}_9 = \frac{\beta^2\hat{\mu}R_I^*\left(1-(1-\varepsilon_{fL})^4\right)}{4\hat{T}\varepsilon_{fL}}$, $\mathbb{R}_{10} = \frac{R_I^*\left(1-(1-\varepsilon_{fL})^5\right)}{15\hat{d}\hat{T}\varepsilon_{fL}}$, $\mathbb{R}_{11} = \frac{\hat{S}\left(1-R_I^*+\tau_{pLs}\right)\left(1-(1-\varepsilon_{fL})^5\right)}{120\varepsilon_{fL}}$, $\mathbb{R}_{12} = \frac{\hat{S}R_I^*\left(1-(1-\varepsilon_{fL})^6\right)}{72\varepsilon_{fL}}$, $\mathbb{R}_{13} = \frac{\left(1-R_I^*+\tau_{pLs}\right)\left(1-(1-\varepsilon_{fL})^5\right)}{120\varepsilon_{fL}}$, $\mathbb{R}_{14} = \frac{R_I^*\left(1-(1-\varepsilon_{fL})^6\right)}{72\varepsilon_{fL}}$.

5.6. Model (vi): Step Function

The basic temperature in this profile drops rapidly by a certain amount ΔT_{fL} at $z_{fL} = \varepsilon_{fL}$ and ΔT_{pL} at $z_{pL} = \varepsilon_{pL}$, otherwise it is uniform. Accordingly,

$$F_{fL}(z_{fL}) = \delta\left(z_{fL}-\varepsilon_{fL}\right) \text{ and } F_{pL}(z_{pL}) = \delta\left(z_{pL}-\varepsilon_{pL}\right) \tag{39}$$

The R_C is attained for this model by utilizing (39) in (31) and is calculated as follows:

$$R_C = \frac{\left(\hat{d}^2+\hat{T}\right)+\left(\hat{d}^2+\hat{S}\right)\tau_{fLs}\tau_{pLs}-\hat{d}^4\kappa_{pLs}^2\tau_{pLs}\Psi_6-R_{pLs}\{\mathbb{R}_{25}+\mathbb{R}_{26}\}}{\hat{T}\{\mathbb{R}_{27}+\mathbb{R}_{28}\}+\left[\alpha_{fpL}\,\kappa_{fpL}^2+\alpha_{spL}\kappa_{spL}^2\tau_{spL}\right]\hat{d}^4\;\Psi_6} \tag{40}$$

where $\Psi_6 = \mathbb{R}_{15}+\mathbb{R}_{16}+\mathbb{R}_{17}+\mathbb{R}_{18}+\mathbb{R}_{19}+\mathbb{R}_{20}+\mathbb{R}_{21}+\mathbb{R}_{22}+\mathbb{R}_{23}+\mathbb{R}_{24}$, $\mathbb{R}_{15} = \frac{\hat{d}^2\beta^2\left(1+R_{IM}^*+\tau_{fLs}\right)\varepsilon_{pL}^2}{2}$, $\mathbb{R}_{16} = \frac{\hat{d}^2\beta^2 R_{IM}^*\varepsilon_{pL}^3}{4}$, $\mathbb{R}_{17} = \frac{\hat{d}^2\beta^2\left(1-R_I^*+\tau_{pLs}\right)}{2\hat{T}}$, $\mathbb{R}_{18} = \frac{\hat{d}\beta^2\hat{\mu}\left(1+R_I^*+\tau_{pLs}\right)\varepsilon_{fL}}{\hat{T}}$, $\mathbb{R}_{19} = \frac{\beta^2\hat{\mu}\left(1-R_I^*+\tau_{pLs}\right)\varepsilon_{fL}^2}{2\hat{T}}$, $\mathbb{R}_{20} = \frac{\left(1-R_I^*+\tau_{pLs}\right)\varepsilon_{fL}^3}{6\hat{d}\hat{T}}$, $\mathbb{R}_{21} = \frac{\hat{d}^2\beta^2 R_I^*\varepsilon_{fL}}{\hat{T}}$, $\mathbb{R}_{22} = \frac{2\hat{d}\beta^2\hat{\mu}R_I^*\varepsilon_{fL}^2}{\hat{T}}$, $\mathbb{R}_{23} = \frac{\beta^2\hat{\mu}R_I^*\varepsilon_{fL}^3}{\hat{T}}$, $\mathbb{R}_{24} = \frac{R_I^*\varepsilon_{fL}^4}{6\hat{d}\hat{T}}$, $\mathbb{R}_{25} = \frac{\hat{S}\left(1-R_I^*+\tau_{pLs}\right)\varepsilon_{fL}^4}{24}$, $\mathbb{R}_{26} = \frac{\hat{S}R_I^*\varepsilon_{fL}^5}{12}$, $\mathbb{R}_{27} = \frac{\left(1-R_I^*+\tau_{pLs}\right)\varepsilon_{fL}^4}{24}$, $\mathbb{R}_{28} = \frac{R_I^*\varepsilon_{fL}^5}{12}$.

6. Results and Discussion

The theoretical investigation focuses on the initiation of TCRB convection in a combined structure. This system comprises a region-I positioned above a region-II that is saturated with the same fluid. The analysis is conducted in accordance with the LTNE model. The analytical calculations and graphical representations are performed utilizing the advanced computational software known as MATHEMATICA, version 11. The eigenvalue

issue is resolved by the utilization of the perturbation method, resulting in the derivation of an analytical expression for the critical Rayleigh number. This expression is obtained for six distinct thermal gradients, as indicated in Table 1. The graph depicts the relationship between the critical Rayleigh number (R_C) and the depth ratio ($\hat{d}$) for all the cases examined in the current study, specifically in the context of adiabatic rigid boundaries. Also, there is a noticeable pattern in the profiles' stability. The range of values under consideration in the present analysis is as follows: $\alpha_{spL} = 2$, $\kappa_{fpL} = 0.2$, $\kappa_{spL} = 0.3$, $\tau_{fLs} = 0.2$, $\tau_{pLs} = 0.3$, $R_{fLs} = 10$, $R_{pLs} = 10$, $\hat{T} = 1.0$, $R_I^* = 0.1$, $R_{IM}^* = 1.0$, $\beta = 1$, $\kappa_{pLs} = 0.5$, $\kappa_{fLs} = 0.3$ and $\alpha_{fpL} = 1$.

The impact of the thermal expansion ratio α_{fpL} on R_C is illustrated in Figure 2. The curves exhibit divergence when considering the values $\alpha_{fpL} = 1$, 5, and 10. The figure clearly demonstrates a positive correlation between α_{fpL} and R_C, indicating that an increase in α_{fpL} results in a corresponding increase in R_C. Consequently, the setup can achieve stability, thereby delaying the onset of TCRB convection. Based on the graph, it can be observed that the linear profile exhibits greater stability compared to the parabolic profile. In comparison, PLHB exhibits greater stability, while SF demonstrates a higher degree of instability. The impact of the parameter is minimal in the parabolic profiles, while it is more pronounced in the linear profiles. According to the data presented in Figure 3, an increase in the variable solid phase expansion ratio α_{spL} leads to a corresponding increase in the R_C. Consequently, this adjustment in the setup has the potential to enhance the stability and delay the onset of TCRB convection. Based on the graph, it can be observed that the linear profile exhibits the highest level of stability, while the parabolic profile demonstrates instability. In a similar vein, it can be observed that PLHB exhibits a higher degree of stability compared to SF, which is relatively less stable. The impact of the parameter is minimal in parabolic profiles, whereas it is more significant in linear profiles. It is observed that nearly equivalent outcomes are achieved for the variables α_{fpL} and α_{spL}. It is evident from Figure 4 that the growth in the porous parameters β leads to a rise in the R_C. Consequently, this allows for the stabilization of the setup, resulting in a delayed onset of TCRB convection. As a result, the system is postponed. The graphs indicate that the linear and PLHB models exhibit greater stability, while the parabolic and SF models demonstrate higher levels of instability. Additionally, the impact of the porous parameter is significantly more pronounced for the linear and PLHB models, moderately significant for the inverted parabolic and PLCA models, and detrimental for the parabolic and SF thermal gradient models. Figures 5 and 6 exhibit the effects of the fluid and solid phase thermal diffusivity ratios, respectively, κ_{fpL} and κ_{spL}. As the ratios increase, R_C increases. As a result, the setup is stable, delaying the onset of TCRB convection. Hence the system is postponed. The effects of the corrected internal Rayleigh numbers R_I^* and R_{IM}^* are illustrated in Figures 7 and 8. The system experiences destabilization as the R_I^* parameter increases, resulting in the earlier occurrence of TCRB convection for higher values of this parameter. The TCRB convection effectively regulates smaller values of the R_I^*. It is observed in Figure 8 that there is an inverse response from the porous layer R_{IM}^*. This enhances the system stability by increasing the value of R_C. The observed curves exhibit a divergence pattern, suggesting that the sensitivity arises when the porous layer predominates over the composite layer across all thermal gradients. Therefore, the TCRB convection is delayed. The influence of the solute Rayleigh numbers R_{fLs} and R_{pLs} over the R_C are depicted in Figure 9 when $R_{fLs} = R_{pLs} = 10, 20, 30$, and 30. With the increase in R_{fLs} and R_{pLs}, R_C decreases, destabilizing the setup. TCRB convection, hence, starts up quickly. The observed phenomenon could potentially arise from the existence of a secondary constituent.

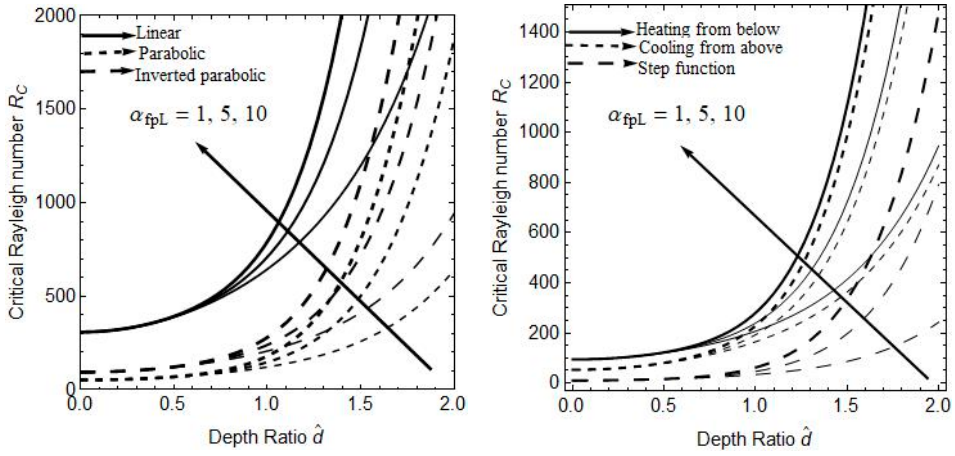

(**a**) (**b**)

Figure 2. The effect of the fluid phase thermal expansion ratio $\alpha_{fpL} = 1, 5, 10$ on R_C. (**a**) Linear, parabolic and inverted parabolic, (**b**) Heating from below, cooling from above and step function.

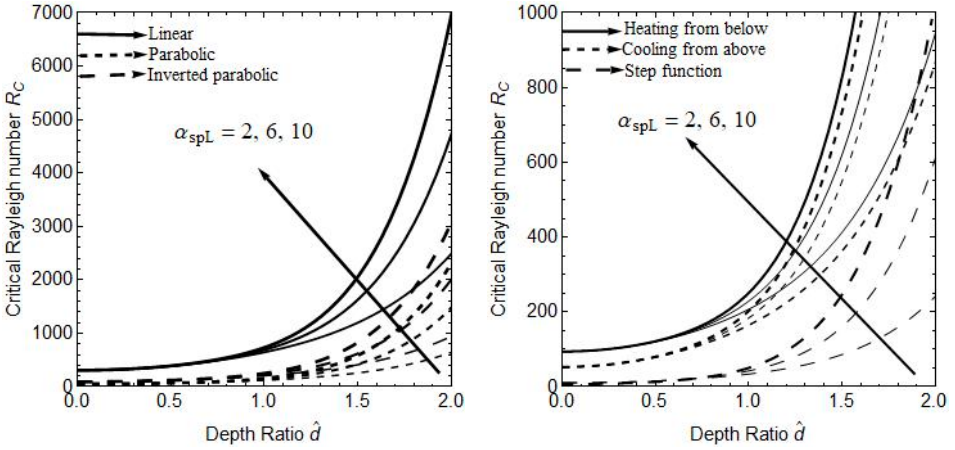

(**a**) (**b**)

Figure 3. Influence of the solid phase thermal expansion ratio $\alpha_{spL} = 2, 6, 10$ on R_C. (**a**) Linear, parabolic and inverted parabolic, (**b**) Heating from below, cooling from above and step function.

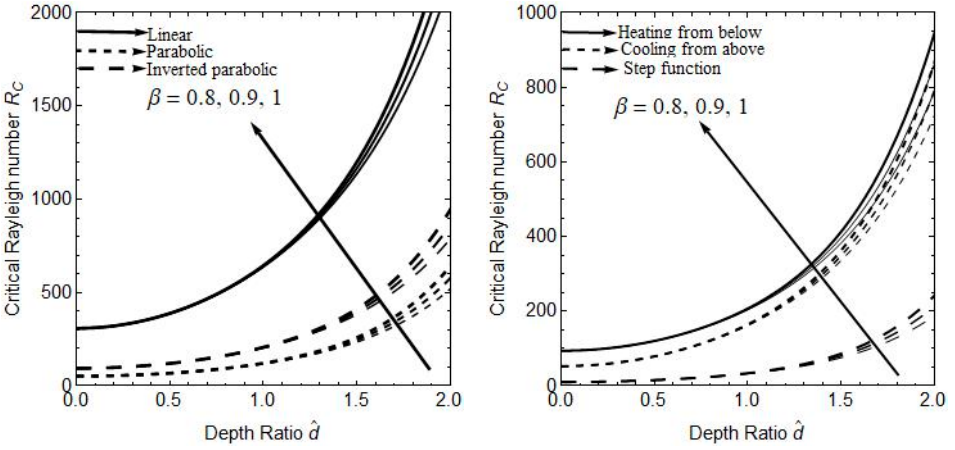

(**a**) (**b**)

Figure 4. Impact of the porous parameter $\beta = 0.8, 0.9, 1.0$ on R_C. (**a**) Linear, parabolic and inverted parabolic, (**b**) Heating from below, cooling from above and step function.

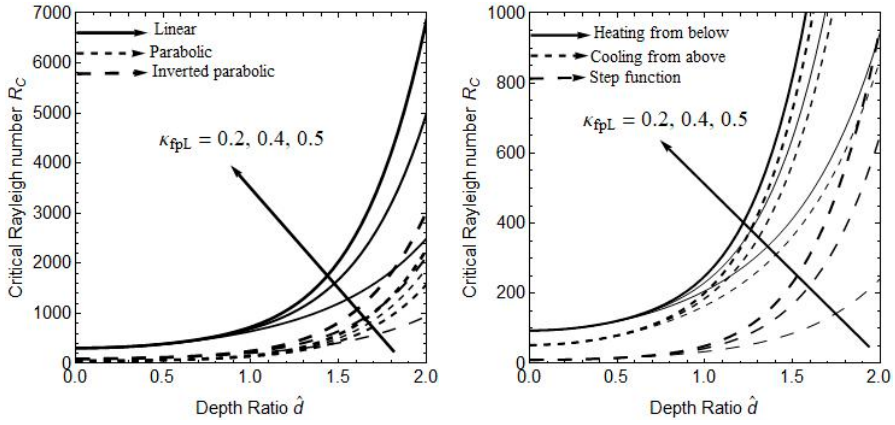

(**a**) (**b**)

Figure 5. The effect of the fluid phase thermal diffusivity $\kappa_{fpL} = 0.2, 0.4, 0.5$, on R_C. (**a**) Linear, parabolic and inverted parabolic, (**b**) Heating from below, cooling from above and step function.

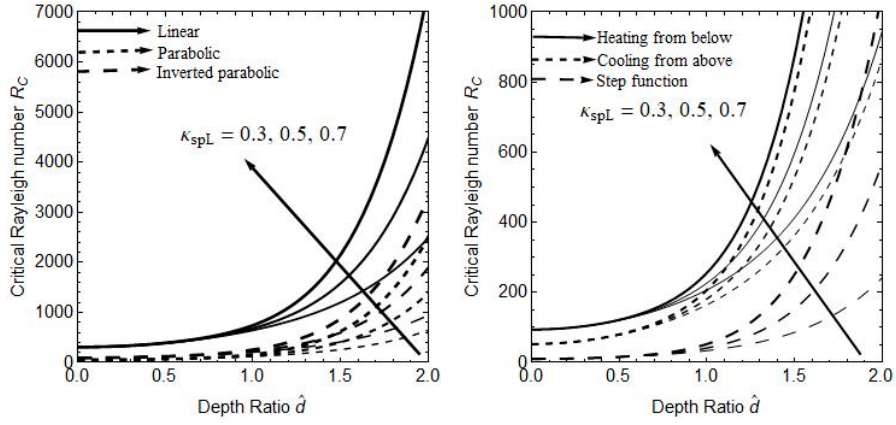

(**a**) (**b**)

Figure 6. The effect of the variation of the solid phase thermal diffusivity ratio $\kappa_{spL} = 0.3, 0.5, 0.7$, on R_C. (**a**) Linear, parabolic and inverted parabolic, (**b**) Heating from below, cooling from above and step function.

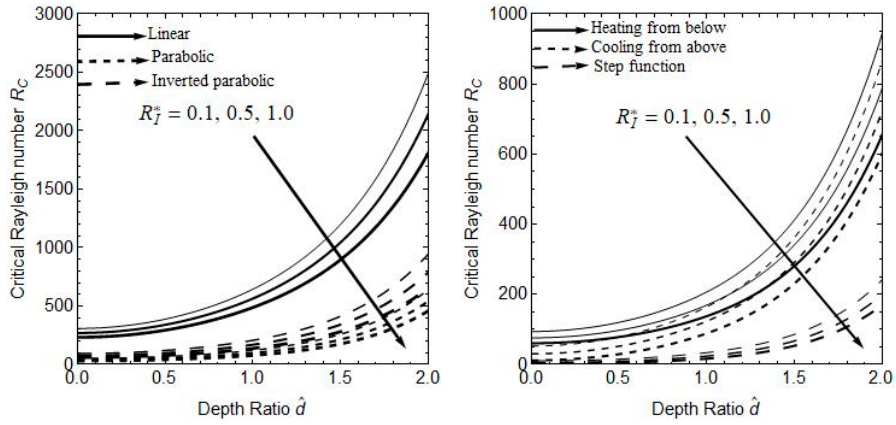

(**a**) (**b**)

Figure 7. Influence of corrected internal Rayleigh number in region-I $R_I^* = 0.1, 0.5, 1.0$ on R_C. (**a**) Linear, parabolic and inverted parabolic, (**b**) Heating from below, cooling from above and step function.

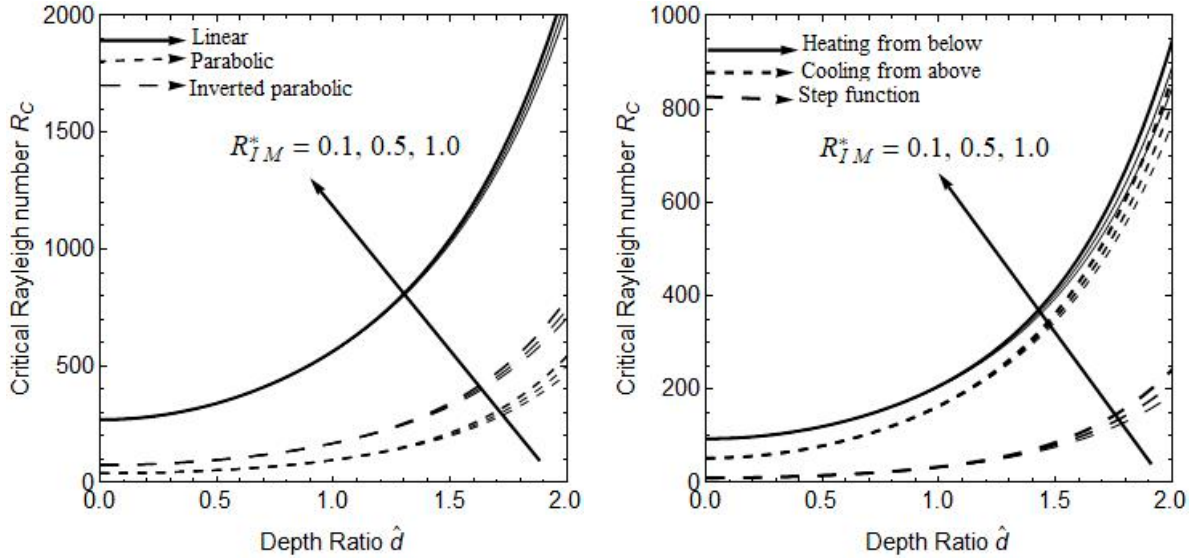

(**a**) (**b**)

Figure 8. The influence of corrected internal Rayleigh number in region-II $R^*_{IM} = 0.1, 0.5, 1.0$ on R_C. (**a**) Linear, parabolic and inverted parabolic, (**b**) Heating from below, cooling from above and step function.

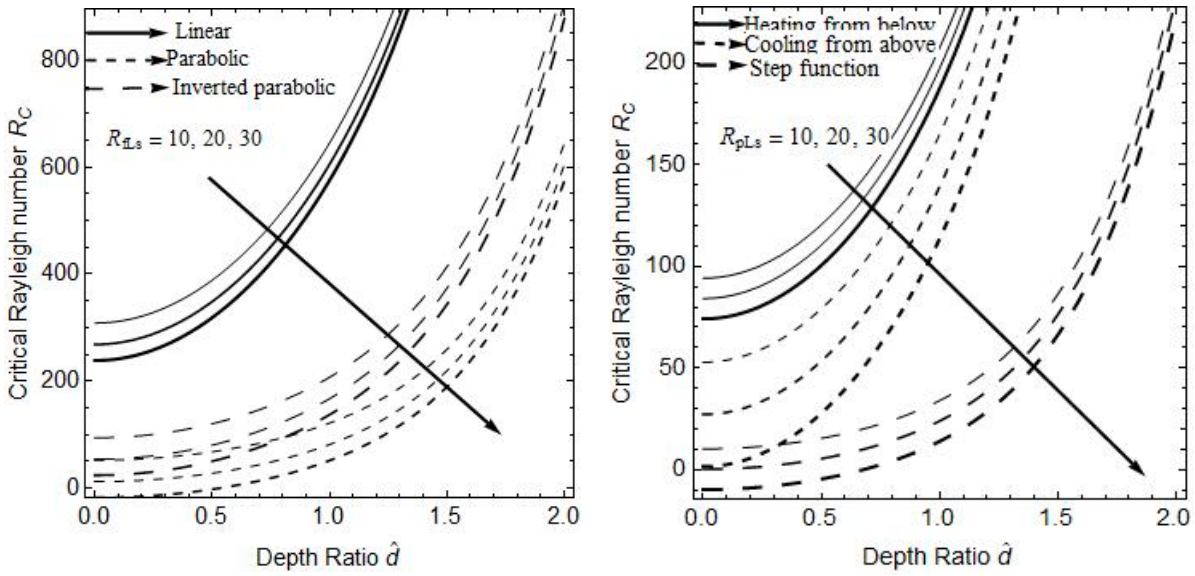

(**a**) (**b**)

Figure 9. Impacts of solute Rayleigh numbers $R_{fLs} = R_{pLs} = 10, 20, 30$ on R_C. (**a**) Linear, parabolic and inverted parabolic, (**b**) Heating from below, cooling from above and step function.

7. Conclusions

The primary focus of this theoretical investigation is the initiation of the two-component Rayleigh–Bènard (TCRB) convection in a combined structure. The system consists of a region-I situated above a region-II that is fully saturated with the same fluid. The analysis is performed following the LTNE model. The present endeavor necessitates the examination of the situation within the framework of arbitrary boundary conditions for salinity and temperature. The eigenvalue problem is solved using the perturbation method, which leads to the derivation of an analytical expression for the critical Rayleigh number. The aforementioned expression is derived from six unique thermal gradients, as outlined in Table 1. The present study has yielded the following outcomes.

(i) The onset of TCRB convection is supported by a corrected internal Rayleigh number in region-I and the solute Rayleigh number. By increasing the system's instability, the six profiles speed up the beginning of TCRB convection with the corrected internal Rayleigh number in region-I and the solute Rayleigh number.
(ii) When applied to each of the six profiles, the thermal ratio, the thermal diffusivity ratio, the porous parameter, and the corrected internal Rayleigh number all work together to postpone the onset of TCRB convection.
(iii) In a combined structure arrangement with region-I on top, the parabolic profile is more stable than the step function, but in a setup with region-II on top, the step function takes the lead.
(iv) The PLHB structure exhibits the highest stability among the combined structures in region-II, whereas the linear structure demonstrates the lowest stability.
(v) The commencement of TCRB convection in a composite fluid and porous layer system may be efficiently controlled by selecting the proper parameters.

Author Contributions: Conceptualization, V.K.B., M.N., S.R. and R.U.; methodology, V.K.B. and M.N.; validation, G.A., M.N., R.U. and G.Y.H.; formal analysis, G.Y.H. and M.N.; investigation, R.U. and G.A.; writing—original draft preparation, G.Y.H., M.N., S.R., V.K.B. and G.A.; writing—review and editing, G.A.; visualization, all the authors; supervision, M.N. and G.A.; project administration, M.N. and R.U.; funding acquisition, G.A. All authors have read and agreed to the published version of the manuscript.

Funding: Princess Nourah bint Abdulrahman University Researchers Supporting Project number **(PNURSP2023R45)**, Princess Nourah bint Abdulrahman University, Riyadh, Saudi Arabia.

Data Availability Statement: Not applicable.

Acknowledgments: Princess Nourah bint Abdulrahman University Researchers Supporting Project number **(PNURSP2023R45),** Princess Nourah bint Abdulrahman University, Riyadh, Saudi Arabia.

Conflicts of Interest: The authors declare no conflict of interest.

Nomenclature

English Letters		**Greek Letters**	
a_{fL}, a_{pL}	Wave numbers	ρ_0	Reference density, kg/m^3
C_{fL}, C_{pL}	Concentrations, mol/m^3	ρ_{fL}, ρ_{pL}	Fluid and porous layer density, kg/m^3
C_0	Reference concentration, mol/m^3	μ_{fL}, μ_{pL}	Fluid viscosity and porous viscosity, kg/ms
C_p	Specific heat capacity, J/kg·K	ΔT	Temperature difference, K
D_{fL}, D_{pL}	$D_{fL} = \frac{d}{dz_{fL}}, D_{pL} = \frac{d}{dz_{pL}}$	ΔC	Concentrate difference, mol/m^3
Da	Darcy number	κ_{fL}, κ_{pL}	Thermal diffusivities in fluid and porous layer, m^2/s
d_{fL}, d_{pL}	Thickness, m	$\kappa_{fLs}, \kappa_{pLs}$	Solute diffusivity ratio
$\hat{d}$	Depth ratio	$\kappa_{pL}, \kappa_{spL}$	Thermal diffusivity of fluid and solid phase in porous layer, m^2/s
g	Gravity, m/s^2	α_{fL}, α_{pL}	Thermal expansion coefficients in fluid and porous layer, 1/K
H	Scaled interface heat transfer coefficient, W/mK	$\alpha_{fpL}, \alpha_{spL}$	Thermal expansion coefficients in fluid and solid phase in porous layer, 1/K
h	Inter-phase heat transfer, W/m^2/K	$\alpha_{fLs}, \alpha_{pLs}$	Solute thermal expansion coefficients in fluid and porous layer, 1/K
K	Permeability, H/m	τ_{spL}	Inter-phase thermal diffusivity ratio, m^2/s

English Letters		**Greek Letters**	
$\hat{k}$	(0, 0, 1)	τ_{fL}, τ_{pL}	Thermal diffusivity ratio, m^2/s
P_{fL}, P_{pL}	Pressure, kg $m^{-1}s^{-2}$	τ_{fLs}, τ_{pLs}	Solute thermal diffusivity ratios, m^2/s
$\vec{q}_{fL}, \vec{q}_{pL}$	Velocity vectors, m/s	θ_{fL}, θ_{pL}	Amplitude of perturbed temperature, K
R_C	Critical Rayleigh number	β	Porous parameter
R_{fLs}, R_{spL}	Solute Rayleigh numbers	ϕ	Porosity
$R_{fL,}R_{pL}$	Rayleigh numbers	$\hat{\mu}$	Viscosity ratio
R_I, R_{IM}	Internal Rayleigh numbers	**Subscripts**	
R_I^*, R_{IM}^*	Corrected internal Rayleigh numbers	b	Basic state
$\hat{S}$	Solute ratio	fL	Fluid layer
S_{fL}, S_{pL}	Amplitude of perturbed concentration	pL	Porous layer
T_{fL}, T_{pL}, T_{spL}	Temperatures, K	fpL	Fluid phase porous layer
T_0	Interface temperature, K	spL	Solid phase porous layer
$\hat{T}$	Thermal ratio	fLs	Fluid layer salinity
W_{fL}, W_{pL}	Dimensionless vertical velocities	pLs	Porous layer salinity
$F_{fL}(z_{fL})$, $F_{pL}(z_{pL})$	Fluid and porous layer temperature gradient		

Appendix A

The zero-order expressions are as follows:

For region-I,

$$D_{fL}^4 W_{fL0} = 0$$

$$D_{fL}^2 \theta_{fL0} + \left[F_{fL}(z_{fL}) + R_I^*\left(2z_{fL} - 1\right)\right] W_{fL0} = 0$$

$$\tau_{fLs} D_{fL}^2 S_{fL0} + W_{fL0} = 0$$

For region-II,

$$D_{pL}^2 W_{pL0} = 0$$

$$\phi D_{pL}^2 \theta_{fpL0} + \left[F_{pL}(z_{pL}) + R_{IM}^*(2z_{pL} + 1)\right] w_{pL0} + H\left(\theta_{spL0} - \theta_{fpL0}\right) = 0$$

$$(1 - \phi) D_{pL}^2 \theta_{spL0} + H\left(\theta_{spL0} - \theta_{pL0}\right) = 0$$

$$\tau_{pLs} D_{pL}^2 S_{pL0} + W_{pL0} = 0$$

The zero-order boundary conditions are as follows:

$$W_{fL0}(1) = 0, D_{fL} W_{fL0}(1) = 0, D_{fL}\theta_{fL0}(1) = 0, \quad D_{fL} S_{fL0}(1) = 0, \hat{T} W_{fL0}(0) = W_{pL0}(1),$$

$$\hat{T}\hat{d} D_{fL} W_{fL0}(0) = \hat{\mu}\, W_{pL0}(1), \theta_{fL0}(0) = \hat{T}\theta_{fpL0}(1), \theta_{fL0}(0) = \hat{T}\theta_{spL0}(1), S_{fL0}(0) = \hat{S} S_{pL0}(1),$$

$$D_{fL} S_{fL0}(0) = D_{pL} S_{pL0}(1), D_{fL}\theta_{fL0}(0) = D_{pL}\theta_{pL0}(1), D_{fL}\theta_{fL0}(0) = D_{pL}\theta_{spL0}(1),$$

$$\hat{T}\hat{d}^2 D_{fL}^2 W_{fL0}(0) = \hat{\mu} D_{pL}^2 W_{pL0}(1), \hat{T}\hat{d}^3 \beta^2 D_{fL}^3 W_{fL0}(0) = D_{pL} W_{fL0}(1) + \hat{\mu}\beta^2 D_{pL}^3 W_{pL0}(1),$$

$$W_{pL0}(0) = 0, D_{pL}W_{pL0}(0) = 0, D_{pL}\theta_{fpL0}(0) = 0, D_{pL}\theta_{spL0}(0) = 0, D_{pL}S_{pL0}(0) = 0.$$

The zeroth-order equations have solutions which are given by

$$W_{fL0}(z) = 0, \theta_{fL0}(z) = \hat{T}, W_{pL0}(z_{pL}) = 0, \theta_{fpL0}(z_{pL}) = 1, \theta_{spL0}(z_{pL}) = 1.$$

$$\delta_{fL1} = \frac{-\hat{d}^2\beta^2\left(R_{fpL} + R_{spL}\,\tau_{spL} - R_{pLs}\,\tau_{pLs}\right)}{2\hat{T}}, \delta_{fL2} = \frac{-\hat{\mu}\hat{d}\beta^2\left(R_{fpL} + R_{spL}\,\tau_{spL} - R_{pLs}\,\tau_{pLs}\right)}{\hat{T}},$$

$$\delta_{fL3} = \frac{-\hat{\mu}\beta^2\left(R_{fpL} + R_{spL}\,\tau_{spL} - R_{pLs}\,\tau_{pLs}\right)}{2\hat{T}}, \delta_{fL4} = \frac{-\left(R_{fpL} + R_{spL}\,\tau_{spL} - R_{pLs}\,\tau_{pLs}\right)}{2\hat{T}},$$

$$\delta_{pL5} = 0, \quad \delta_{pL6} = 0.$$

References

1. Wang, P.; Vafai, K.; Liu, D.Y. Analysis of radiative effect under local thermal non-equilibrium conditions in porous media-application to a solar air receiver. *Numer. Heat Transf. Part A Appl.* **2014**, *65*, 931–948. [CrossRef]
2. Altawallbeh, A.A.; Hashim, I.; Tawalbeh, A.A. Thermal non-equilibrium double diffusive convection in a Maxwell fluid with internal heat source. *J. Phys. Conf. Ser.* **2018**, *1132*, 012027. [CrossRef]
3. Altawallbeh, A.A.; Hashim, I.; Bhadauria, B.S. Magneto-double diffusive convection in a viscoelastic fluid saturated porous layer with internal heat source. *AIP Conf. Proc.* **2019**, *2116*, 030015. [CrossRef]
4. Abidin, N.H.; Mokhtar, N.F.; Majid, Z.A. Onset of Bènard-Marangoni instabilities in a double diffusive binary fluid layer with temperature dependent viscosity. *Numer. Algebra Control Optim.* **2019**, *9*, 413–421. [CrossRef]
5. Komala, B.; Sumithra, R. Effects of non-uniform salinity gradients on the onset of double diffusive magneto—Marangoni convection in a composite layer. *Int. J. Adv. Sci. Technol.* **2019**, *28*, 874–885.
6. Kuznetsov, A.V.; Nield, D.A. Effect of local thermal non-equilibrium on the onset of convection in a porous medium layer saturated by a nanofluid. *Transp. Porous Med.* **2010**, *83*, 425–436. [CrossRef]
7. Thumma, T.; Mishra, S.R. Effect of nonuniform heat source/sink, and viscous and Joule dissipation on 3D Eyring–Powell nanofluid flow over a stretching sheet. *J. Comput. Des. Eng.* **2020**, *7*, 412–426. [CrossRef]
8. Prabha, G.S.; Bharathi, M.C.; Kudenatti, R.B. Heat transfer through mixed convection boundary layer in a porous medium: LTNE analysis. *Appl. Therm. Eng.* **2020**, *179*, 115705. [CrossRef]
9. Kannan, R.M.; Pullepu, B. Numerical solutions of double diffusive convective flow past a chemical reactive vertically inclined infinite plate with heat source/sink. *Adv. Math. Sci. J.* **2020**, *9*, 1623–1636. [CrossRef]
10. Astanina, M.S.; Sheremet, M.; Umavathi, C.J. Unsteady natural convection in a partially porous cavity having a heat-generating source using local thermal non-equilibrium model. *Int. J. Numer. Methods Heat Fluid Flow* **2019**, *29*, 1902–1919. [CrossRef]
11. Hema, M.; Shivakumara, I.S.; Ravisha, M. Double diffusive LTNE porous convection with Cattaneo effects in the solid. *Heat Transf.* **2020**, *49*, 3613–3629. [CrossRef]
12. Nadian, P.K.; Pundir, R.; Pundir, S.K. Study of double–diffusive convection in a rotating couple stress ferromagnetic fluid in the presence of varying gravitational field and horizontal magnetic field saturating in a porous medium. *J. Math. Comput. Sci.* **2021**, *11*, 1784–1809.
13. Shukla, S.; Gupta, U. LTNE effects on triple-diffusive convection in nanofluids. *ASME J. Heat. Transf.* **2022**, *144*, 092501. [CrossRef]
14. Mahajan, A.; Tripathi, V.K. Stability of a chemically reacting double-diffusive fluid layer in a porous medium. *Heat Transf.* **2021**, *50*, 6148–6163. [CrossRef]
15. Meften, G.A.; Ali, A.H. Continuous dependence for double diffusive convection in a Brinkman model with variable viscosity. *Acta Univ. Sapientiae Math.* **2022**, *14*, 125–146. [CrossRef]
16. Capone, F.; Gianfrani, J.A. Natural convection in a fluid saturating an anisotropic porous medium in LTNE: Effect of depth-dependent viscosity. *Acta Mech.* **2022**, *233*, 4535–4548. [CrossRef]
17. Capone, F.; Gianfrani, J.A. Thermal convection for a Darcy–Brinkman rotating anisotropic porous layer in local thermal non-equilibrium. *Ric. Mat.* **2022**, *71*, 227–243. [CrossRef]
18. Abed Meften, G.; Ali, A.H.; Al-Ghafri, K.S.; Awrejcewicz, J.; Bazighifan, O. Nonlinear stability and linear instability of double-diffusive convection in a rotating with LTNE Effects and symmetric properties: Brinkmann-Forchheimer model. *Symmetry* **2022**, *14*, 565. [CrossRef]
19. Akram, S.; Athar, M.; Saeed, K.; Umair, M.Y. Nanomaterials effects on induced magnetic field and double-diffusivity convection on peristaltic transport on Prandtl nanofluids in inclined asymmetric channel. *Nanomater. Nanotechnol.* **2022**, *12*, 18479804211048630. [CrossRef]

20. Tayebi, T.; Dahmane, F.; Jamshed, W.; Chamkha, A.J.; El Din, S.M.; Raizah, Z. Double diffusive magneto-natural convection of nano fluid in an enclosure equipped with a wavy porous cylinder in the local thermal non-equilibrium situation. *Case Stud. Therm. Eng.* **2023**, *43*, 102785. [CrossRef]
21. Siddabasappa, C.; Siddehwar, P.G.; Mallikarjunaih, S.M. Analytical study of Brinkman-Bènard convection in a bidisperse porous medium: Linear and weakly nonlinear study. *Therm. Sci. Eng. Prog.* **2023**, *39*, 101696. [CrossRef]
22. Noon, N.J.; Haddad, S.A. Stability Analysis of double diffusive convection in local thermal non-equilibrium porous medium with Internal heat source and reaction effects. *J. Non-Equilib. Thermodyn.* **2023**, *48*, 25–39. [CrossRef]
23. Corcione, M.; Quintino, A. Double-Diffusive effects on the onset of Rayleigh-Benard convection of water-based nanofluids. *Appl. Sci.* **2022**, *12*, 8485. [CrossRef]
24. Gangadharaiah, Y.H.; Manjunatha, N.; Udhayakumar, R.; Almarri, B.; Elshenhab, A.M.; Honnappa, N. Darcy–Brinkman double diffusive convection in an anisotropic porous layer with gravity fluctuation and throughflow. *Mathematics* **2023**, *11*, 1287.
25. Mehdy, A.N. Double diffusive free convection in a packed bed square enclosure by using local thermal non-equilibrium model. *J. Eng.* **2023**, *18*, 121–136. [CrossRef]
26. Jakhar, A.; Kumar, A. Instability analysis of double diffusive convection under time dependent solute boundary conditions in the presence of internal heat generator. *Phys. Fluids* **2023**, *35*, 077101. [CrossRef]
27. Yellamma; Narayanappa, M.; Udhayakumar, R.; Almarri, B.; Ramakrishna, S.; Elshenhab, A.M. The impact of heat source and temperature gradient on Brinkman–Bènard triple-diffusive magneto-Marangoni convection in a two-layer system. *Symmetry* **2023**, *15*, 644. [CrossRef]
28. Rudolph, P.; Wang, W.; Tsukamoto, K.; Wu, D. Transport phenomena of crystal growth-heat and mass transfer. *AIP Conf. Proc.* **2010**, *1270*, 107–132.
29. Sumithra, R.; Venkatraman, S. Local thermal non-equilibrium dominant Darcy-Rayleigh-Bènard-magneto-Marangoni convection in a composite layer. *J. Mines Met. Fuels* **2022**, *70*, 1–12. [CrossRef]
30. Nield, D.A.; Bejan, A. *Convection in Porous Media*, 3rd ed.; Springer: New York, NY, USA, 2006.
31. Manjunatha, N.; Khan, U.; Elattar, S.; Eldin, S.M.; Chohan, J.S.; Sumithra, R.; Sarada, K. Onset of triple-diffusive convective stability in the presence of a heat source and temperature gradients: An exact method. *AIMS Math.* **2023**, *8*, 13432–13453.
32. Rudraiah, N.; Veerappa, B.; Balachandra, R.S. Effects of nonuniform thermal gradient and adiabatic boundaries on convection in porous media. *J. Heat Transf.* **1980**, *102*, 254. [CrossRef]
33. Vasseur, P.; Robillard, L. The Brinkman model for natural convection in a porous layer: Effects of nonuniform thermal gradient. *Int. J. Heat Mass. Transf.* **1993**, *36*, 4199. [CrossRef]
34. Shivakumara, I.S. Onset of convection in a couple-stress fluid-saturated porous medium: Effects of non-uniform temperature gradients. *Arch. Appl. Mech.* **2010**, *80*, 949–957. [CrossRef]